Artificial halos

Markus Selmke[a)]
Institute for Experimental Physics I, Universität Leipzig, 04103 Leipzig, Germany

(Received 3 December 2014; accepted 22 June 2015)

Judged by their frequency and beauty, ice halos easily rival rainbows as a prominent atmospheric optics phenomenon. This article presents experimental halo demonstrations of varying complexity. Using a single commercially available hexagonal glass prism, a variety of artificial halos can be simulated. The experiments include laser beam path analysis, a modified classic spinning prism experiment, and a novel Monte-Carlo machine for three-dimensional rotations. Each of these experiments emulates different conditions of certain halo displays, and in combination, they allow a thorough understanding of these striking phenomena. © *2015 American Association of Physics Teachers.*
[http://dx.doi.org/10.1119/1.4923458]

I. INTRODUCTION

Atmospheric optics phenomena associated with refraction provide instructive examples for the concepts of geometrical optics. For instance, the formation of a rainbow by rain drops is a classic example in standard optics courses.[5,6] In contrast, ice halos receive much less attention than rainbows, even though they can be observed year-round by the alert observer, appearing on average twice a week in parts of the United States and Europe.[1–3] Instead of being formed by liquid rain drops, ice halos are caused by hexagonal ice crystals; they require high clouds or cold air harboring the crystals.

The most frequent ice halos are the 22° parhelia (PH). They originate from the refraction of sunlight through platelike crystals that have their hexagonal faces oriented parallel to the horizon, while their orientations about the vertical axis are random, as sketched in Fig. 1(a). Light passing through the side faces of these crystals experiences a minimum deviation of $\gtrsim 22°$. The inclination angle e of such rays towards the horizon does not change, much in the same way that a ray is transmitted through a vertical wedge prism without change in inclination.[35] (A proof of this statement is given in Appendix A.) Accordingly, the parhelia appear as two bright spots at $\gtrsim 22°$ left and right from the sun at solar elevation, giving them their more colloquial name "sun dogs." Since blue colors are refracted more than red colors, the parhelia have a reddish tint towards the sun.

By the same mechanism, hexagonal column-like ice crystals of completely random orientations produce the circular 22° *halo* (ring) around the sun; see Fig. 1(d). Still by the same ray paths through the crystals, but due to crystals having their long axis parallel to the horizon as their only orientational constraint [Fig. 1(c)], tangent arcs or the circumscribed halo result. Depending on the ice crystal orientations that are realized and hydrodynamically stable under certain weather conditions,[7] many more delicate arcs and circles may decorate the sky.

The mechanisms involved for each halo phenomenon may include refraction and/or (internal) reflection(s), leading to some colored and some colorless ice halos. More extensive accounts of the diverse halo phenomena and additional photographs can be found in numerous books[1,2,8] and on Cowley's web site.[3] While truly complex displays with a combination of several halo types are more rare, a bit of luck and some patience is enough to see displays such as the one shown in Fig. 2.

Ever since the pioneering work of Bravais in 1847,[9,10] rotating single prisms have been used in laboratory experiments to simulate ice halo phenomena.[11–15] In an extension of previous experiments, a series of artificial halo experiments can be realized; they involve basic concepts of geometrical and wave optics and bring ice-halo science to students in undergraduate or graduate courses in optics. Further new demonstrations are limited only by the creativity of the experimentalist in bringing about certain prism rotations.

II. CAUSTICS AND FAKE CAUSTICS

The formation of parhelia shares many aspects with the formation of a rainbow. For a single spherical object, such as a drop of water, a true caustic appears when it is illuminated with parallel light. Here, a caustic refers to the diverging intensity pattern at the envelope of the focused family of all possible rays.[8,16] The rainbow caustic is a result of ray paths that involve two refractions and one internal reflection by the surface of the sphere. Due to dispersion a caustic appears for each color, giving rise to the colored caustic seen in Fig. 3(a).[5,6,17] The angle of this caustic, which can be predicted using geometrical optics, determines where the individual drops must be relative to the observer and the sun, such that they contribute to the rainbow perceived by that observer.

For ice halos, the situation is different in one detail. A single hexagonal crystal of fixed orientation does not show by itself any divergent intensity pattern under illumination, and thus no caustic; see Fig. 3(b). Aside from dispersion, which plays a role for certain light paths, only parallel bundles of rays leave the flat prism faces and appear as columns of light emerging from an illuminated prism. However, incoherent averaging over orientations can generate a geometric singularity in the intensity pattern that is similar to a caustic; see Fig. 4. This phenomenon is known as a fake-caustic.[12,18,38] In analogy to the formation of a rainbow, the net sum of many glints from ice crystals with a statistical distribution of orientations then causes certain halos to be perceived by an observer. A halo is thus the collective effect of many crystals with different orientations.

An experimental approach to simulate such halos must therefore include some way of averaging orientations. One way to achieve this goal is to use a host of artificial prisms. To this end, a variety of chemical recipes have been put forward with limited success.[13,19,20,37] A more controlled method consists in the use of macroscopic prisms.[1,9,11,13–15]

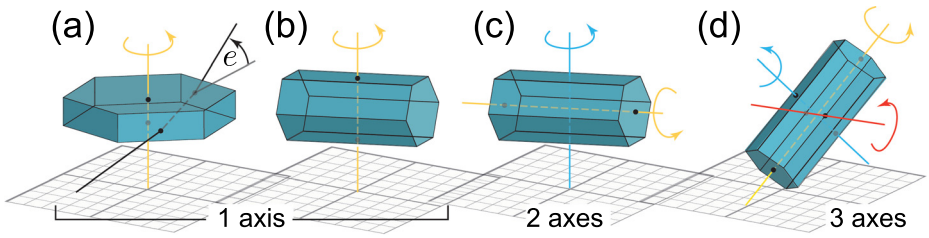

Fig. 1. Ensembles of crystals with different orientational degrees of freedom are responsible for different halos. (a) Oriented plates (horizontal orientation) → parhelia, parhelic circle, circumhorizontal, and circumzenithal arc. A parhelion ray path is depicted, incident at an angle e relative to the horizon plane (grid). (b) Parry oriented columns → Parry arcs. (c) Singly oriented columns → circumscribed halo/tangent arcs. (d) Randomly orientated columns, rotation about three perpendicular axes → circular 22° halo. Only some of the most common resulting halos are listed here (Refs. 1–3).

While this technique precludes the use of many prisms for practical reasons, an orientational sampling can be accomplished through physical rotation of a single prism. High-quality glass prisms are commercially available through optics suppliers such as Edmund Optics. They owe their availability to their ability to spatially homogenize the output light distribution of sources such as LEDs through multiple internal reflections.[21] Although the index of refraction of BK7 glass, $n = 1.52$, is different from that of ice $n = 1.31$, the dispersion is similar.[22] Longer wavelengths (red colors) experience a slightly lower index of refraction than shorter wavelengths (blue colors). Consequently, the coloring of the halos, while appearing at different angles, is qualitatively similar. Despite several discrepancies between glass halos and ice halos (no birefringence), their common physical principles and overall features make them an appealing field of study. Alternatively, water-filled prisms can be used to better approximate ice crystals.[9,11,14]

III. ARTIFICIAL PARHELIA AND PARHELIC CIRCLES

Mounting a bare prism centrally on an axial ball bearing (and preferably some inertial mass, see Fig. 5), a single spinning hexagonal prism will average over all in-plane orientations as indicated in Fig. 1(a). Alternatively, an electric drill can be used to rotate a prism, or a thread can be attached with a rubber band or suction cup to the prism to suspend it and set it in rotation. Such an experiment simulates the large ensemble of horizontally oriented hexagonal ice crystals that together cause the colored parhelia at both sides of the sun.[1,2,9,12,13,15] Illuminating a rotating prism with a white light source making an angle e with the supporting table mimics a nonzero solar elevation and generates a light pattern as shown in Fig. 4. The illumination can be masked such that only the prism is illuminated (see inset). Setting a long exposure for the camera accomplishes the necessary time-averaging.

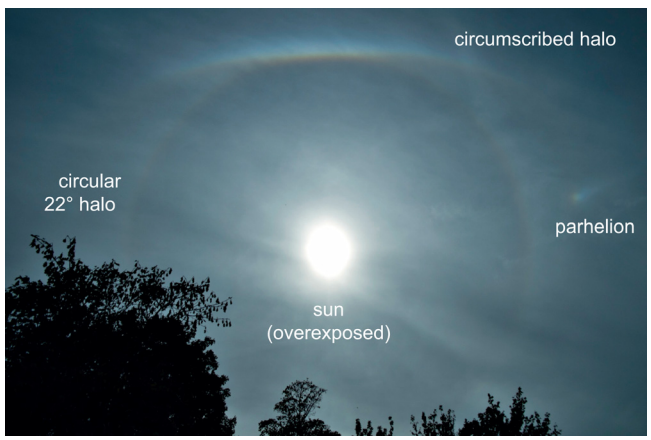

Fig. 2. Photo of a complex halo display (September 24, 2014, 1:29 p.m., Leipzig, Germany; camera: Fuji X-E1, $f = 18$ mm, aperture set to $f/4.0$, 65° horizontal angle of view) with solar elevation $e \approx 38°$. The image was post-processed using unsharp masking. Visible are the right parhelion, the circular 22° halo, and the / upper tangent arc circumscribed halo. Such images can be reproduced by simulation software (i.e., HaloSim, Ref. 4) to determine the responsible ice crystal ensembles. Here, referring to Fig. 1, the ensemble is approximately 15% orientation (a), 45% orientation (c), and 40% orientation (d). The simulated image is shown in Appendix B along with an un-enhanced version of the photo (Fig. 12).

The faces that are responsible for the refraction causing the PH are separated by one face. Such pairs of faces enclose a prism angle of $\gamma = 60°$, as shown in the sketch in Fig. 4. The general expression for the angle of minimum deviation through a prism reads[9,35]

$$\theta_{\mathrm{PH}}(e) = 2\arcsin\left[n(e)\sin\left(\frac{\gamma}{2}\right)\right] - \gamma. \tag{1}$$

This is the limiting angle of the fake caustic generated by a rotating prism or an ensemble of horizontally oriented ice prisms as viewed from a fixed position being the coordinate center; see Fig. 4. In fact, the theoretical intensity distribution of the PH—the corresponding fake caustic—shows a divergence as $\propto 1/\sqrt{\theta - \theta_{\mathrm{PH}}}$ close to the PH halo angle.[12,18,23]

The nonzero elevation angle e of the sun or light source changes the geometry of the situation. As long as the incident ray is within the same plane, it suffices to consider the 2D-projected geometry of the refraction through a horizontal prism. If the incident ray makes an angle relative to this horizontal plane (the supporting table), the full 3D geometry must be considered instead. However, refractions by vertical interfaces of the prism can be decomposed into refractions within the horizontal plane and a vertical plane. It turns out that the 2D-projected refractions within the horizontal plane, (as sketched in the inset of Fig. 4 and photographed in Fig. 6), are then described by an effective index of refraction given by

$$n(e) \to \frac{\sqrt{n^2 - \sin^2(e)}}{\cos e}. \tag{2}$$

This is the so-called Bravais index of refraction for inclined rays.[9,35] A derivation of this result is given in Appendix A. For natural ice, the PH angle Eq. (1) is $\theta_{\mathrm{PH}} \approx 22°$ at low solar elevations and gradually increases with increasing

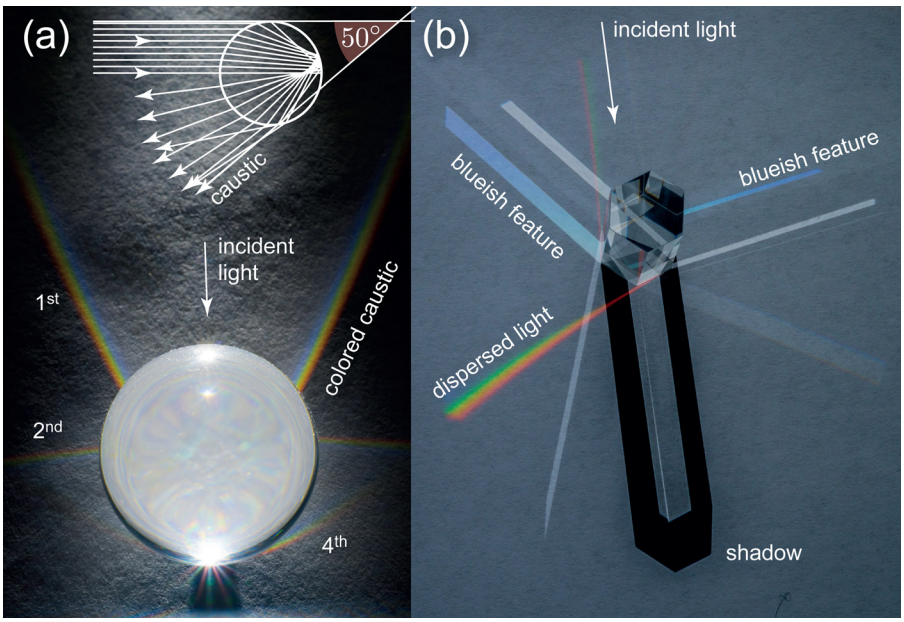

Fig. 3. (a) Photograph of caustics (boundaries between bright and dark regions) due to an acrylic sphere illuminated by parallel white light. The rainbow caustic (see inset) corresponds to the first-order rainbow, while other caustics give rise to higher-order rainbows (Refs. 5 and 6). Here, the cone of the 3D rainbow caustic makes an angle ≈50° and intersects the plane upon which the sphere rests. The light source elevation is approximately zero and situated towards the top of the image. (b) Illumination of a static hexagonal glass prism (height $h = 45$ mm, edge length $l = 11.55$ mm) yields no caustics. The light source elevation was $e \approx 29°$. Both photos have been enhanced in vibrance, saturation and contrast by 40%.

elevation e. In Fig. 2, the solar elevation was $e \approx 38°$, and accordingly the visible right parhelion appears outside of the circular 22° halo at an azimuth of $\theta_{PH} \approx 34°$. (In general, the apparent angular distance of each parhelion to the sun is *not* the azimuth coordinate θ_{PH}; see Appendix B for details.)

Red colors are refracted less than blue ones ($n_r = 1.307$ and $n_b = 1.317$), and hence the PH appears reddish towards the sun. The effect of non-parallel light may further be considered and removes the strict divergence of the caustic.[23] Nonetheless, the perceived angular extent of the natural PH is also related to the chromatic dispersion of the angular peak position. This dispersion, as described by Eq. (1), is about 1.1° for ice. For the demonstration experiment, the macroscopic dimension of the prism further increases the width of the projected PH feature. For the BK7 glass material, the refractive index is higher and results in a larger characteristic angle $\theta_{PH}(e) \geq 39°$; see Fig. 4.

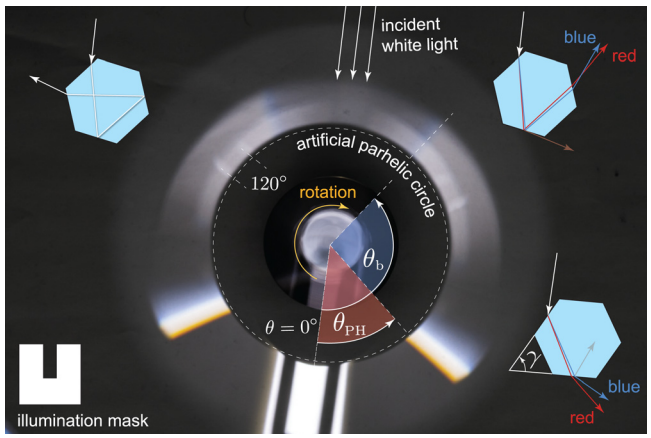

Fig. 4. Artificial parhelia embedded in a parhelic circle (image by Sarah Borchardt). Long exposure image of a rotating prism illuminated by a flashlamp at an elevation $e \approx 31°$. A mask was used to illuminate the prism only. Characteristic azimuths are the parhelia angle $\theta_{PH}(e)$ and the limiting angle $\theta_b(e)$ of the bluish feature. The responsible ray paths are sketched. The 120° PH appear as two bright columns inclined accordingly and at approximately the same azimuth.

Inspection of the experiment immediately reveals that the prominent parhelia are embedded in a fainter intensity pattern. This azimuthal pattern along the dashed circle in Fig. 4 is the artificial counterpart to what is called the parhelic circle (PHC) halo, which appears as an intensity distribution at sun-elevation and may span the entire azimuthal range of the sky.[1–3] While this natural halo is rarely seen in its entirety, segments of it are more common, as seen in Fig. 7. Dedicated simulation tools, written in the programming language *Processing*,[24] are provided as an electronic supplement to this paper.[25] These tools allow a real-time simulation of the artificial PHC intensity and color pattern for any elevation e, as predicted by geometrical optics. Each feature in the intensity distribution can be attributed to one or several ray paths of the incident light through the crystal.

An accompanying investigation of these paths using a focusable laser diode helps to understand their corresponding features. Each of them is determined by geometrical constraints and partial as well as total reflections. A series of photographs of characteristic ray paths is shown in Fig. 6. The use of a blue diode laser makes the internal beam paths visible via autofluorescence of the prism material. Consecutive segments may or may not be equal in brightness, depending on whether the internal reflection was total or partial. Since every ray path is reversible, the inverse succession of face encounters is possible for each as well. Slowly turning the prism allows one to directly see how certain exiting rays behave. For instance, the ray responsible for either PH spends most of its time at the minimum deflection angle. This angle serves as a turning point, such that on average these rays contribute to the diverging intensity under this

Fig. 5. Brass rotary stage with a shaft fitted to the top race of an axial (thrust) ball bearing at its bottom. The lower race and the balls of the bearing rest on a supporting table. The 5-mm-deep rectangular ($2l \times \sqrt{3}\,l$) milled recess fits the prism of Fig. 3(b).

angle. That is to say, they contribute to the fake caustic and make up the PH. Somewhat less intense, but clearly visible, is a bluish feature at about 140°, seen in Fig. 4. This feature is due to the contribution from the ray paths sketched next to it and photographed in Fig. 6. For this path, a steep increase of the intensity due to the onset of a total internal reflection at the second interface occurs at a characteristic azimuth angle θ_b, given by

$$\theta_b(e) = \frac{\pi}{3} + 2\arcsin\left\{n\sin\left[\frac{\pi}{3} - \arcsin\left(\frac{1}{n}\right)\right]\right\}. \qquad (3)$$

A derivation of this result is given in Appendix C, where it is shown that the ray path involves no net refraction. Irrespective of the index of refraction, the deflection angle for any ray of light along this path is the same. However, the wavelength dependence of the refractive index of BK7 glass still causes this characteristic angle to be larger for blue than for red light. A bluish edge is the result of the earlier increase in intensity for blue light in this ray path due to total internal reflection. Again, a separate investigation using a diode laser can be used to demonstrate this mechanism. In fact, arriving at this conclusion and the particular ray path responsible for the blue feature is a worthwhile student exercise. Incidentally, two ray paths of similar intensity cover the corresponding azimuthal range. However, only one of them allows for the total internal reflection mechanism to limit its azimuthal range in the backwards direction, while the other one is limited by geometric constraints for large deviation angles. Slowly moving the prism and observing the corresponding ray's behaviors will eventually give the correct answer. Interestingly, a very similar mechanism based on color-dependent total internal reflection is responsible for the natural rare blue spot halo.[26]

The structure of the artificial PHC further shows that not all segments that contribute to the azimuthal pattern have the same radial extent. The explanation for this can be found by observing the lengths of the light columns emerging from a statically illuminated prism. A longer ray path through the prism corresponding to a particular light column will cause it to intersect the table closer to the prism. Therefore, external reflections, for instance, produce the longest columns and upon rotational averaging the farthest extending dim outer

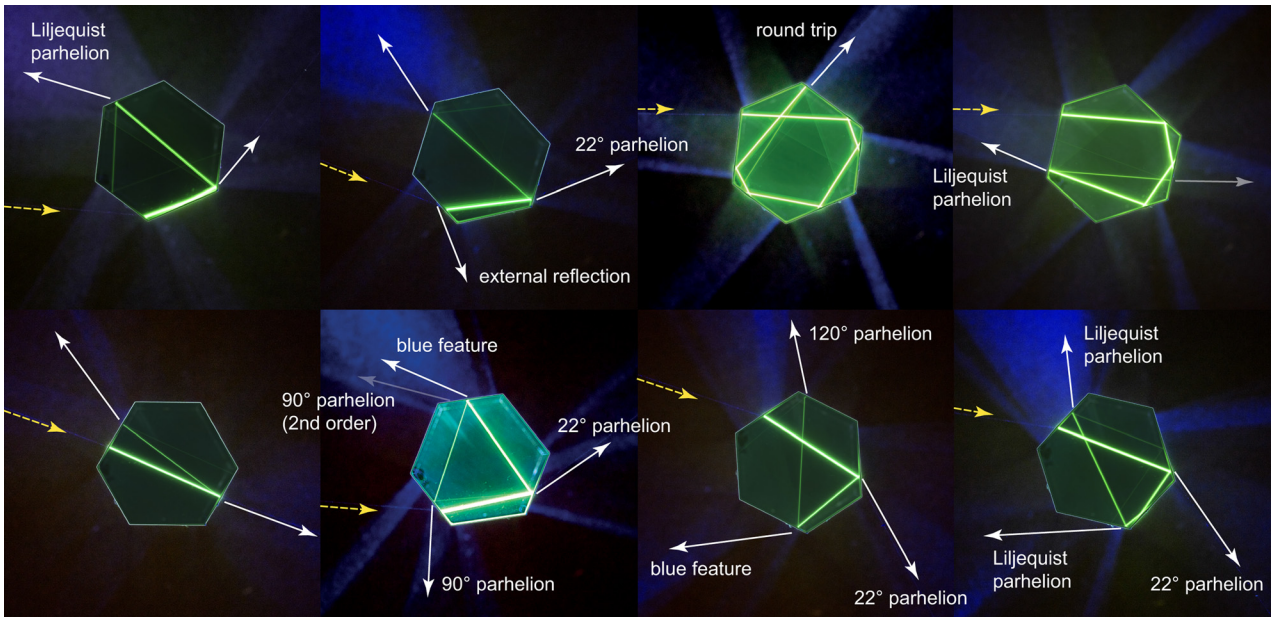

Fig. 6. Various ray paths through the hexagonal glass prism as seen from above, with zero light source elevation. A focusable diode laser operating at a wavelength $\lambda = 405$ nm was used to make the beam visible via autofluorescence. The exterior of the prism was exposure-corrected via image processing to make the incident direct free-space beam visible (dashed yellow arrows). The white arrows indicate various exiting rays and are annotated by the features/halos they are responsible for. Most of these weaker beams are not visible in free space. Images were captured in RAW format using a Fuji X-E1 camera equipped with the Fujinon XF 60 mm F2.4 R macro lens (ISO200, aperture $f/6.4$, 20–30 s exposure). Rays responsible for the 120° parhelia are deflected by this angle for any prism orientation.

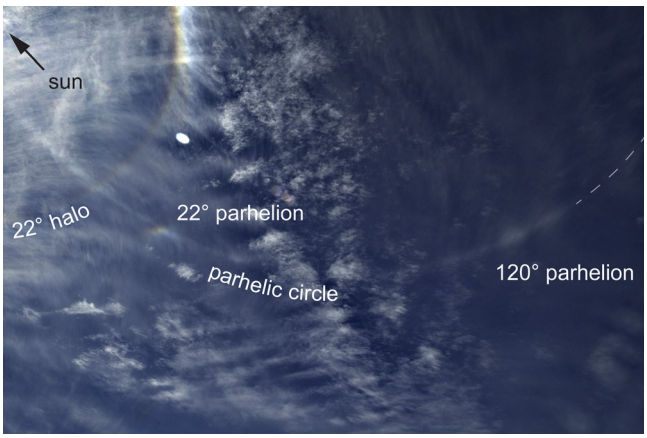

Fig. 7. Photo ($f = 14$ mm, aperture $f/14$, August 1, 2015, 11:30 a.m., Berkholz-Meyenburg, Germany) of a parhelic circle (PHC) segment at solar elevation $e \approx 50^\circ$. The photo was enhanced for clarity.

circular pattern (see Fig. 4). Taking images of the rotating prism at different light source elevations e, one can extract the characteristic azimuth angles for each PHC feature. This was done for Fig. 8 using the simple table-top setup of Fig. 4. The theoretical dependence on elevation e as given by Eqs. (1) and (3), along with Eq. (2), is shown as solid lines and reasonably agrees with the experimental data. The systematic deviations are due to the nonzero size of the prism; they disappear when a distant screen instead of the supporting table is used for the PHC projection.

Alternatively, a static prism experiment can also be used to obtain plots as in Fig. 8. For each light source elevation e, the orientation of the prism would be changed carefully to observe the minimum deviation angle of the forward refracted light to get θ_{PH}. To find the angle θ_b, the prism would be reoriented until two bluish light columns emerge, and measuring the deflection of the longer one; cf. Fig. 3(b). The elevation can be obtained using the length s of the shadow and the prism height h, i.e., via $e = \arctan(h/s)$.

Under closer inspection, the experimentally observed PHC intensity pattern reveals several more distinct features apart from the PH and the blue edge. These features are due to different, and at times complex, paths through the prism. Figure 6 shows a selection of such paths, several of which are responsible for the numerous light columns seen in Fig. 3(b). The 120° PH, a white spot-like brightening on the natural PHC, is due to particularly interesting paths involving no net refraction and a constant deflection irrespective of the prisms orientation towards the eponymous azimuth. For the particular contributing path photographed in Fig. 6, the ray deflection is 240°, as shown in Appendix C. Two accordingly inclined features are visible in the artificial PHC in Fig. 4. Further features include the colored first- and second-order 90° PH[9] (occurring at $120^\circ - \theta_{\mathrm{PH}}$ and $120^\circ + \theta_{\mathrm{PH}}$, respectively), the Liljequist PH,[1,27] external reflections, a further blue edge [occurring at $240^\circ - \theta_b$, see Appendix C and the thin blue column of Fig. 3(b)], and round trips. The simple experiment, therefore, offers a plethora of phenomena to be discovered and understood.[36]

A direct comparison to the natural PHC is, however, spoiled by more than just the difference in refractive index and thereby the different azimuths of certain features. More importantly, certain paths that dominate the appearance of the natural halo are impossible for glass prisms. This is true especially at high solar elevations,[1] as can be inferred from full three-dimensional simulations. These paths are for rays that enter through the top prism face and leave through the sides or bottom after internal reflection. Indeed, such rays are responsible for the display of Fig. 7, and for most 120° parhelia.[1–3] The high refractive index of glass being larger than $n > \sqrt{2}$ prevents such trajectories via total internal reflection.[13]

For the same reason, the circumhorizontal and the circumzenithal arc[1–3] cannot be generated using a glass prism (in air), although water-filled prisms can be used to overcome this limitation. (A method to construct such a prism is described in Appendix D.) On a more positive note, several different Parry arcs[1–3] can be obtained by rotating a glass prism with its hexagonal faces vertical and lying flat on one side face;[13,15] cf. Fig. 1(b). While the corresponding ice halos are rather rare in nature, they allow for an easy and spectacular experimental demonstration. Subsuns, the subparhelic circle, and subsun parhelia can be simulated using a spinning thin prism with polished hexagonal faces,[11,15] adding to the accessible halo phenomena using only a single rotation axis. Mildly more complicated two-axis rotation devices can be used to simulate the two degrees of freedom describing singly oriented crystals;[14,15] see Fig. 1(c). Those machines have been shown to readily produce the tangent arcs or the circumscribed halo that is seen in Fig. 2.

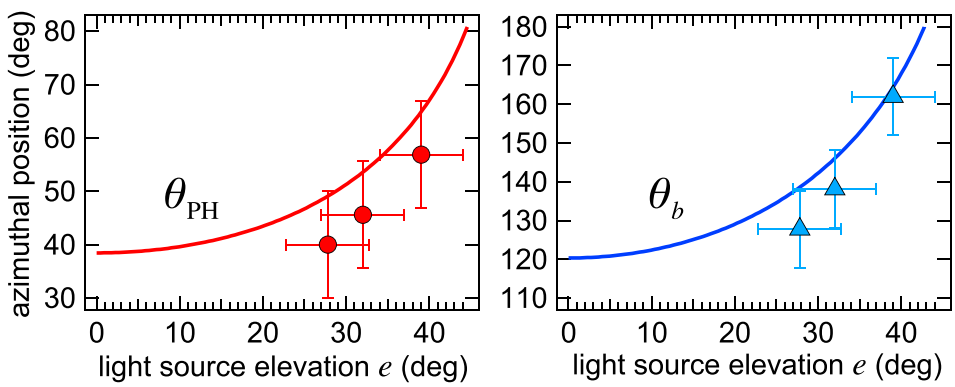

Fig. 8. Expected [Eqs. (1) and (3)] vs measured azimuthal positions for the parhelion and the blue feature on the PHC of Fig. 4. The dependence on the light source elevation e is mediated by the index of refraction $n(e)$ for inclined rays, Eq. (2). Three different light source elevations were used. The systematic offsets are due to the finite distance to the prism.

IV. ARTIFICIAL CIRCULAR 22° HALO VIA A RANDOM WALK MACHINE

To generate the artificial counterpart of the natural circular 22° ice halo around the sun, using only a single hexagonal column prism, the prism must sample all 3D orientations uniformly. This task is similar to the Monte Carlo computer simulations currently used to study ice halo phenomena. Physically, these orientations can be brought about either deterministically or by a succession of random reorientations.[28] The latter mechanism can be implemented rather easily by an Arduino project as shown in Fig. 9. The hexagonal prism (Edmund optics, 20 mm width, cut to 45 mm length) was fixed inside a hollow 80-mm-diameter two-part separable acrylic sphere using fitted rubber pieces (e.g., pieces from an eraser). The hollow sphere itself does not refract the light noticeably if the wall thickness is reasonably thin (<1 mm);[29] it remains basically invisible, similar to a large soap bubble. The sphere and thereby the prism is then rotated about three independent axes by three stepper motors arranged triangularly with mounting brackets as shown in the inset of Fig. 9. To do so, the NEMA-17-sized stepper motors, equipped with 5–10 mm aluminum flex shaft couplers and $\varnothing = 18$ mm rubber O-rings, are randomly actuated in collective modes as indicated by the arrows in the inset. In each mode, all three motors are actuated simultaneously at the same stepping rate. (No attempt has been made to avoid minor skidding of the sphere.) The motor control is done via a USB-programmable Arduino Uno R3 micro controller stacked with two added motor shields, all powered by a power adapter (9 V dc, 1000 mA). Except for the O-rings and the acrylic sphere, these components were purchased from Adafruit.[30] An additional acrylic stage was added to fix the setup.

While it is readily seen that the sphere randomly samples all orientations when in operation, it is interesting to see the connection to a random walk on a triangular lattice.[31] Indeed, each point on the sphere will rotate either forward or backward in directions separated by 120°. For each step, this is equivalent to translations by integer multiples of 60° on a triangular lattice on the sphere. The mean squared angular distance for a point on the sphere is, therefore, given by $\langle \vartheta^2 \rangle = na^2$, with n being the number of reorientations (steps) and a being the angular distance of each reorientation. Complete randomization of the prism orientation is reached if the averaging time is large enough to allow a sufficient number of reorientations such that $\vartheta^2 \gg (4\pi)^2$. Then the entire surface of the sphere is covered by the random walk of any fixed point on the sphere.

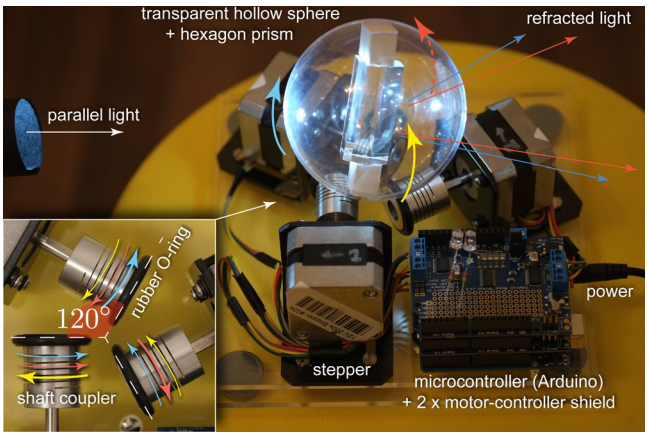

Fig. 9. Random walk halo machine based on an Arduino microcontroller equipped with two motor shields controlling the stepper motors (each controlling up to two steppers, microstepping mode). The sphere-mounted prism is rotated about three axes by different collaborative stepper motor rotation modes (colored arrows; reverse modes not depicted). The random walk samples all possible orientations of the prism, thereby generating the circular 22° halo, as seen in Fig. 10.

Figure 10 shows the sum of $N = 200$ photographs recorded at 30-s intervals using an intervalometer and a Fuji X-E1 digital camera. The machine was set to randomly reorient the sphere by about $a \sim 20°$, about ten times per interval. The number of frames was chosen to assure a homogeneous randomization and sufficient sampling, while still showing the individual contributions of the glints, which in their sum make up the 22° circular halo. The number of frames also depends on the distance to the screen, since it determines the size of the individual glints; in the experiment this distance was about 1 m. An animation of the time-evolution of the averaging and the individual images is provided in the electronic supplement.[25]

In contrast to the azimuth of the PH, the angular radius of the circular 22° ring halo is independent on the light source elevation e (see Fig. 2). This is because the circular halo is caused by prisms having all possible orientations such that the minimum of Eq. (1) determines the resulting fake caustic, the nature of which is however fundamentally different from the parhelia.[38] As a consequence, the circular halo for BK7 glass will have an angular radius of about 39°. The theoretical intensity distribution of this ring halo is given by Eq. (52) of Ref. 23. However, no attempt has been made to verify the prediction, since this would have required capturing and processing a large number of RAW image files.[32]

Complex halo displays like the one shown in Fig. 2 can be obtained by pre-selecting appropriate orientations of the prism before the average of their corresponding projected glints is computed.[33] A practical implementation consists in marking the two ends at which the prism axis exits the hollow sphere. The image containing the marker's projection can then be used to find the orientation. With the help of this information, image subsets can be created to emulate particular ensembles of crystal orientations. Specifically, the circular halo, the circumscribed halo, and the parhelia should thereby be obtainable. Weighted combinations would result in complex artificial halo displays akin to Fig. 2.

More controlled[34] or faster ways to rotate a prism-holding sphere could be used to further improve this experiment.

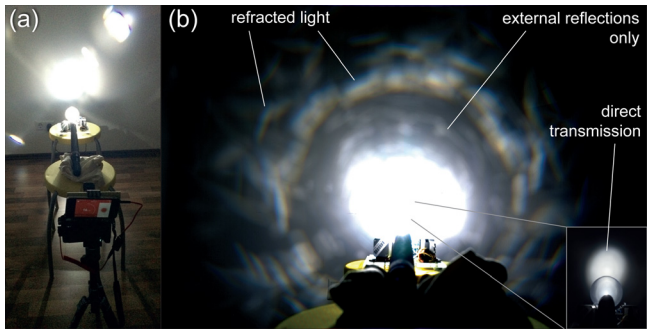

Fig. 10. Artificial circular 22° halo. (a) Setup for the random walk halo machine using a flash lamp and a tripod-mounted camera equipped with an intervalometer. (b) Average of $N = 200$ camera images. (A movie and a maximum projection image is available online (Ref. 25).)

Very recently, a combination of pneumatic and electronic methods was employed to construct a sophisticated machine that rapidly rotates a prism in a cardanic mount about all three axes.[15]

V. CONCLUSION

Ice halos are frequent and impressive atmospheric optics phenomena. The formation principles of a variety of distinct halos provide an interesting application of the laws of geometrical optics. Fake caustics, partial and total internal reflection, refraction, and the deviation of a beam through a prism play important roles. From a scientific viewpoint, hands-on physical experiments on artificial halos allow the investigation of certain characteristics and thereby complement the more common computer simulation approach. From a student's point of view, a recourse to experiments of the type shown in this article should be a satisfying experience. These experiments add a frequent but often unnoticed natural phenomenon to the student's repertoire. Once aware of this phenomenon and encouraged to (always shading their eyes from direct sunlight!) look for it, students quickly begin to notice halo displays on their own. Hopefully, artificial halo experiments of the kind presented here inspire new and creative ways to bring about prism orientations. Halos otherwise too faint to be observed against the bright background of the natural sky could also be visualized by artificial means.

ACKNOWLEDGMENTS

Financial support of Professor F. Cichos and Professor H. Yang is acknowledged. The rotary stage and the acrylic prism were manufactured by the workshop of the department of experimental physics of the Universität Leipzig, Germany. Additional support by S. Borchardt is acknowledged. This work was further supported by a fellowship within the Postdoc-Program of the German Academic Exchange Service (DAAD).

APPENDIX A: EFFECTIVE INDEX OF REFRACTION FOR INCLINED RAYS

When a ray of light making an angle φ with respect to the surface normal $\hat{\mathbf{n}}$ encounters a dielectric interface, Snell's law ($\sin\varphi = n_0 \sin\varphi'$) will determine the refraction and thereby the interior angle φ' measured with respect to the normal. Here, n_0 denotes the constant index of refraction of the material the light ray enters. In order to find the relation between the xy-projection ϕ of the incidence angle and the refracted counterpart ϕ', the sketch in panels (a) and (b) of Fig. 11 can be used. Without loss of generality, the normal vector is set to $\hat{\mathbf{n}} = \hat{\mathbf{e}}_\mathbf{x}$, and the normalized incident ray vector to $\hat{\mathbf{i}} = \{\cos\phi \sin e_c, \sin\phi \sin e_c, \cos e_c\}$. The spherical coordinates' polar angle $e_c = \pi/2 - e$ is introduced here for convenience and related to the elevation angle e. To simplify the mathematics, one can imagine the refracted ray to be on the side of the reflected ray, such that $\hat{\mathbf{r}} = \{\cos\phi' \sin e'_c, \sin\phi' \sin e'_c, \cos e'_c\}$. Now a system of equations is set up. The first equation relates the angles, reading $\hat{\mathbf{r}} \cdot \hat{\mathbf{n}} = \cos\phi' \sin e'_c = \cos[\measuredangle(\hat{\mathbf{r}}, \hat{\mathbf{n}})] = \cos\varphi'$. In this equation, the right-hand side can be related to the incidence angles using $\hat{\mathbf{i}} \cdot \hat{\mathbf{n}} = \cos\varphi = \cos\phi \sin e_c$ and Snell's law as given before. A second equation can be obtained by requiring the ray to remain within the plane of incidence [orange plane in Fig. 11(b)], i.e., $\hat{\mathbf{r}} \cdot (\hat{\mathbf{i}} \times \hat{\mathbf{n}}) = 0$. The system of equation then reads

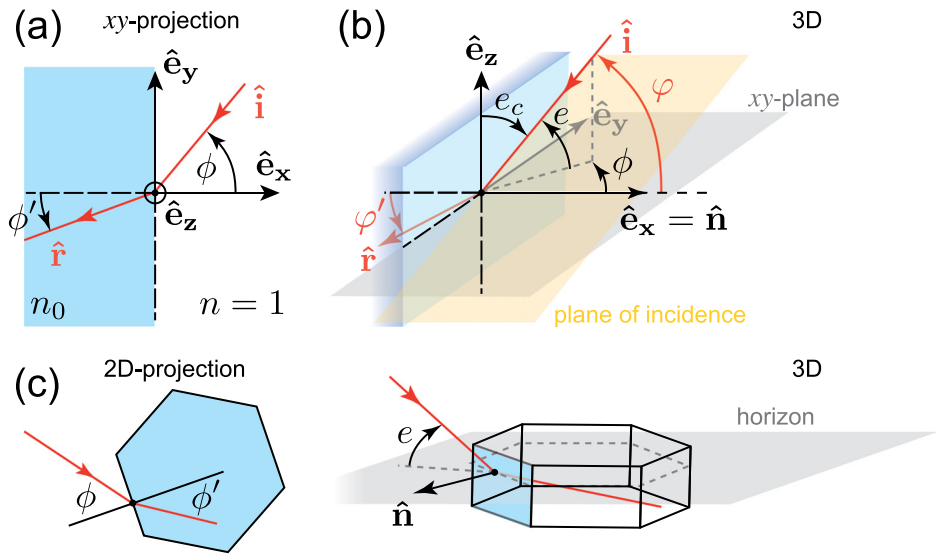

Fig. 11. Refraction by a vertical interface: (a) Projection of the refraction geometry in the xy-plane; only in-plane angles ϕ and ϕ' appear, with a relation yet to be determined. (b) 3D geometry of the same situation. The incident light ray $\hat{\mathbf{i}}$ makes an angle e relative to the xy-plane (gray) and an angle φ relative to the normal $\hat{\mathbf{n}}$. (c) Projected and 3D geometry of refraction by a horizontal crystal (hexagonal face parallel to xy-plane).

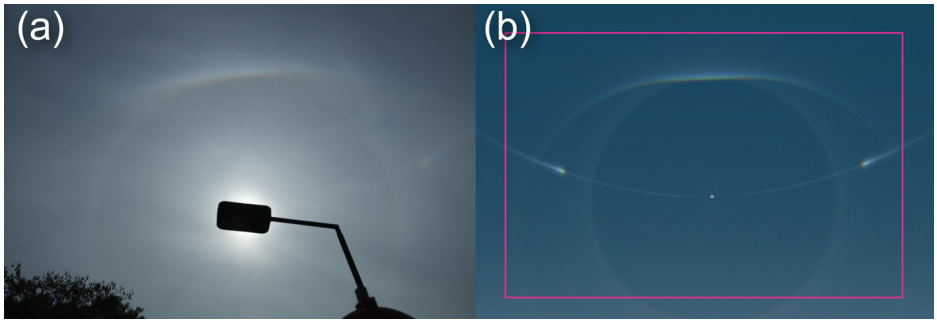

Fig. 12. (a) Unedited photo of the same halo display as in Fig. 2. The sun is blocked by a street light. (b) HaloSim (Ref. 4) simulation adjusted to recreate the display; cf. Appendix B. The rectangle indicates the camera frame size.

$$\cos\phi' \sin e'_c = \sqrt{1 - \frac{1 - \cos^2(e)\cos^2(\phi)}{n_0^2}}, \tag{A1}$$

$$\cos e \cos e'_c \sin\phi - \sin e \sin e'_c \sin\phi' = 0. \tag{A2}$$

This system can be solved for the two unknowns e'_c and ϕ', starting, for instance, by substituting Eq. (A1) into Eq. (A2) and solving for $\cos^2(e'_c)$ after squaring the equation, and using $\cos^2 + \sin^2 = 1$ repeatedly. One finds the elevation to change upon refraction according to $n_0 \sin e' = \sin e$, such that Snell's law directly holds. For two refractions through the crystal faces, i.e., the ray $\hat{\mathbf{r}}$ hitting a second interface with reversed refractive index contrast [cf. Fig. 11(c)], the two refractions cancel and result in no net change in elevation of the exiting ray.[35] This applies to the discussed ray paths contributing to the PHC, including the PH ray at finite light source elevation [cf. Fig. 1(a)].

Now, substituting $\cos e'_c$ back into Eq. (A1) and evaluating $n(e) = \sin\phi / \sin\phi'$, one finally arrives at the desired effective index of refraction for the 2D horizontally projected angles, i.e., Bravais' result,[9] Eq. (2).

Figure 11(c) shows the connection with the refraction through a horizontal hexagonal prism. The horizon corresponds to the xy-plane (gray plane) and is parallel to the hexagonal prism faces; cf. also Fig. 1(a). The solar elevation e describes the angle of the incident rays relative to the horizontal plane, while the side faces represent the refracting vertical interfaces. In a table-top experiment, e corresponds to the inclination angle of the flash lamp or the diode laser with respect to the table upon which the upright prism rests. The projected ray path can be treated as if it were happening in 2D, taking into account the effective index of refraction $n(e)$, Eq. (2); that is, $n(e)\sin\phi' = \sin\phi$ holds for all 2D in-plane refractions. In particular, this applies to the ray path considerations leading to the PH azimuth angle θ_{PH} and those of Appendix C.

APPENDIX B: FULL RAY-TRACING SIMULATION

The photograph of Fig. 2 can be reproduced using the free program HaloSim[4] with the following parameters: 3×10^6 simulated rays, solar elevation 38°, 0.5° light source dispersion, simulation rendering set to user-centered camera view, altitude 44°, azimuth −2°, and a 35-mm-equivalent focal length of 27 mm (set in the camera view box accessible via the tools menu). The following crystals should be set up: 45% horizontal columns (0.1° dispersion, $c/a = 2$), 40% random orientation ($c/a = 2$), 15% plate oriented (1° dispersion, $c/a = 0.2$). Here, c/a denotes the aspect ratio of the ice prisms, with low values indicating plate-like and large values indicating column-like ice prisms.[4] Figure 12 shows a comparison of the simulation with the photographs and gives a reasonable correspondence, although the left parhelion as well as the parhelic circle were absent or too weak to be observed in the display (no appropriate crystals in these regions).

Except for zero solar elevation, the apparent angular distance of each parhelion to the sun is *not* the azimuth coordinate $\theta_{\mathrm{PH}}(e)$. Instead, it is the angle Δ_0 of the great circle segment that the sun S and a parhelion S'.[35] Consider the right spherical triangle on the sky sphere consisting of the following 3 sides (see Fig. 13): Zenith to sun ZS, sun to midpoint between sun and parhelion SM, and this midpoint to the zenith MZ. The law of sines may then be applied to find $\Delta_0 = 2\arcsin[\cos(e)\sin(\theta_{\mathrm{PH}}/2)] < \theta_{\mathrm{PH}}$. Specifically, for the given parameters one finds $\Delta_0 \approx 27°$, thereby fitting well within the camera's field of view.

APPENDIX C: RAY PATH ANALYSIS

For the artificial parhelic circle of glass prisms, three different ray paths are responsible for the most striking features, as shown in Fig. 14. The behavior of the parhelia ray can easily be understood by its equivalence to the refraction through an equilateral prism, as discussed in the main text. The blue edge that bounds a bright segment towards the forward direction is a further notable feature, seen in Fig. 4. Under static illumination, this corresponds to a long and thick blue column emanating from the prism when oriented accordingly, as was done for Fig. 3(b). To calculate this column's in-plane inclination angle relative to the forward direction, or the azimuth θ_b of the blue feature in the PHC, the responsible ray path depicted in Fig. 14(a) must be considered.

The in-plane incidence angle on the relevant prism side face is $\phi_1 = \pi/3 - \delta$. The internal angle ϕ'_1 is related by Snell's law to this angle, i.e., $n(e)\sin\phi'_1 = \sin\phi_1$. Using the constant sum of angles in a triangle, the internal angle at the second interface is found to be $\phi'_2 = \pi/3 - \phi'_1$. Partial transmittance leads to the exiting parhelia ray, while the reflection leads to a third side-face encounter under an internal angle $\phi'_3 = \phi'_1$, whereby $\phi_3 = \phi_1$. The total deviation angle for the ray upon exit is given by $\theta = \phi_1 - \phi'_1 + (\pi - 2\phi'_2) + \phi_3 - \phi'_3 = \pi - 2\delta$. The absence of any dependence on the

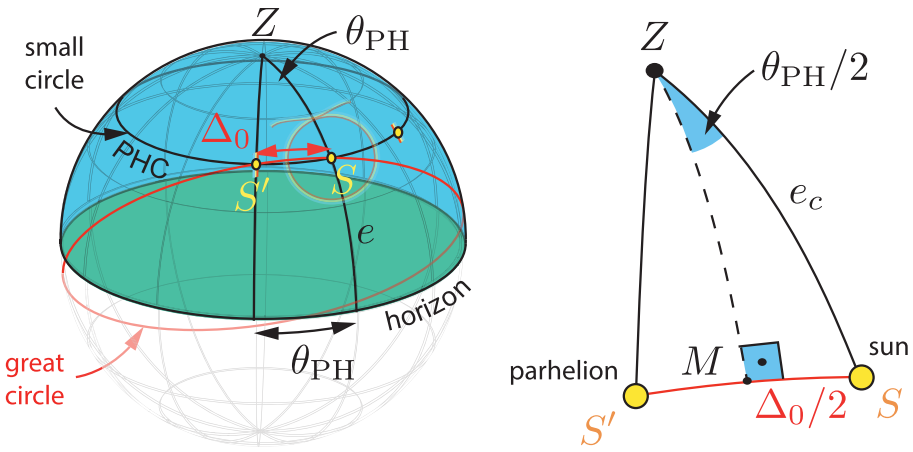

Fig. 13. Sketch illustrating the difference between apparent angular distance Δ_0 from the sun and azimuth θ_{PH} of the parhelion at finite solar elevation. The law of sines for the right spherical triangle *ZMS* reads $\sin(\theta_{PH}/2)/\sin(\Delta_0/2) = \sin(90°)/\sin(e_c)$. The small circle may be lit by the parhelic circle (PHC) halo.

index of refraction indicates that this path, in contrast to the parhelia ray, experiences no net refraction. The blue edge occurs at an azimuth corresponding to the prism orientation δ_b at which the second internal encounter becomes a total internal reflection, i.e., when $\phi_2' = \arcsin[1/n(e)]$. For this orientation, the parhelia ray will no longer exit the prism. When this happens for blue light, red light is still only partially reflected since $n_b > n_r$. As a consequence, within the PHC a transition in color and saturation from white to cyan can be observed with increasing deflection angle. If the light source has some degree of divergence, the same transition of colors can be seen within the bluish light column exiting a static prism; cf. Fig. 3(b). Simple manipulation shows that the orientation is $\delta_b = \pi/3 - \arcsin[n(e)\sin\{\pi/3 - \arcsin[1/n(e)]\}]$. To experimentally check this relation, the light reflected externally in the forward direction can be used [see Fig. 14(b)]. The corresponding ray is deflected by an angle of $\theta_r = \pi/3 - 2\delta$, which can be measured by a triangular ruler to find the prism orientation $\delta \in [0, \pi/6]$. Finally, the particular orientation δ_b can be translated into the azimuth $\theta_b(e) = \theta(\delta = \delta_b)$, resulting in Eq. (3).

A third colored feature is a blue edge bounding a white segment towards the forward direction. A corresponding short and thin blue column may be observed [see Fig. 3(b)]. This feature is due to the path sketched in Fig. 14(b) and photographed in Fig. 6, entering the prism through the same face. Now, for the same orientation δ_b, the two equivalent internal reflections at the second and fourth encountered faces become total internal reflections. The corresponding azimuth is again found from the total angular deviation, here being $\theta = 5\pi/3 - 2\delta_b$. Since the deviation is larger than π, the observed azimuth is $\pi - (\theta - \pi) = \pi/3 + 2\delta_b = 4\pi/3 - \theta_b$. The color is an even purer blue because the selective blue light's total reflection in combination with only partial reflection of red light occurs twice for this path.

The 120° PH ray sketched in Fig. 14(a) and photographed in Fig. 6 experiences a total deflection by $\theta = \phi_1 - \phi_1' + (\pi - 2\phi_2') + (\pi - 2\phi_3') - (\phi_1 - \phi_1') = 4\pi/3$, irrespective of the prism orientation δ and showing no dispersion. By the same argument as above, the observed azimuth is $2\pi/3$ (120°). Due to geometrical constraints, this path may only be possible for a certain range of orientations δ depending on $n(e)$.

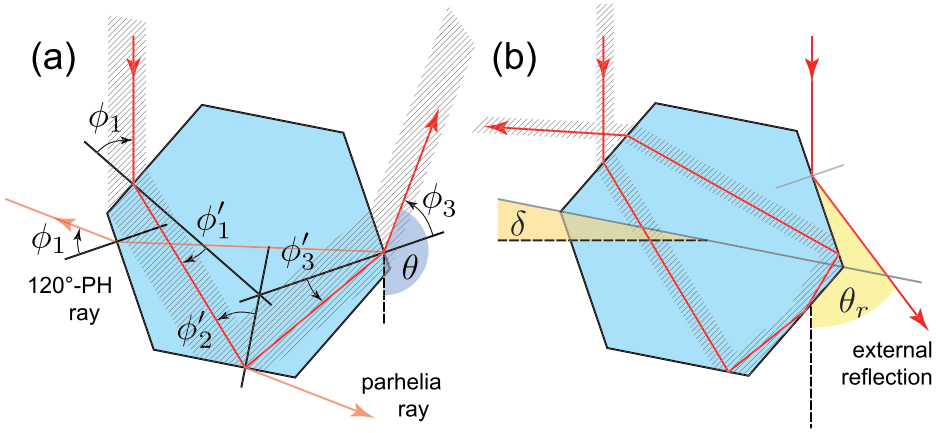

Fig. 14. (a) The ray path corresponding to the thick and long blue column of light in Fig. 3(b) experiences a deviation by $\theta = \pi - 2\delta$, which explains the blue feature around θ_b in the artificial PHC; cf. Fig. 4. The shaded area marks a parallel bundle of rays traversing the same path. (b) The prism orientation δ determines the angular deviation $\theta_r = \pi/3 - 2\delta$ of the forward-reflected light. The sketched ray patch corresponds to the thin and short blue column of light in Fig. 3(b).

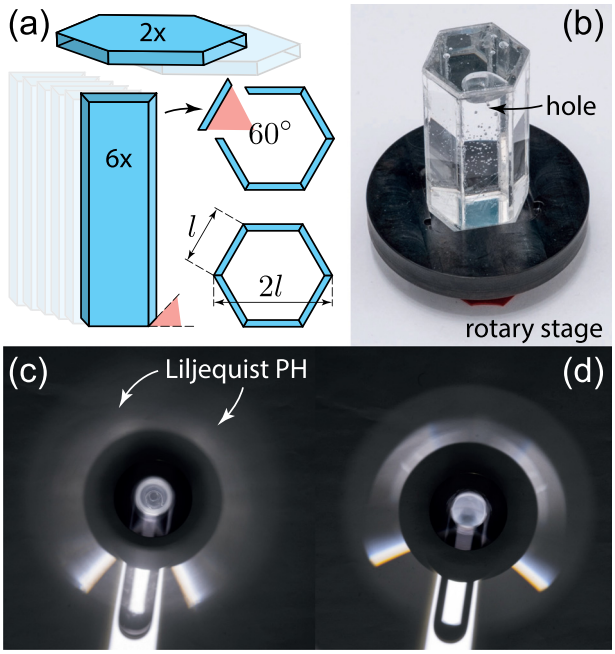

Fig. 15. (a) Construction plan for a water-filled prism. (b) Prism made from acrylic glass, assembled with glue; wall thickness is 1.5 mm and side length is $l = 11.55$ mm. (c) Artificial PHC at $e \approx 31^\circ$ for the water-filled prism, showing the Liljequist PH contribution due to the ray path of Fig. 14(b). (d) BK7 glass PHC for comparison. Images taken by Sarah Borchardt.

Reference 36 contains characteristic azimuth values for further features on the PHC. It also describes a quantitative theoretical description of the PHC intensities based on ray analysis similar to the above treatment of the most important contributing ray paths.

APPENDIX D: WATER PRISM

A prism that can be filled with water can be constructed according to the instructions of Fig. 15(a). Eight pieces are required, ideally machined to produce accurately angled side faces; an acrylic version is shown in Fig. 15(b). A small hole with a diameter of ∼1 mm in one of the side faces can be used in combination with a syringe to fill the prism after assembly. Capillary forces prevent leakage of the water. Figure 15(c) shows artificially generated Liljequist parhelia on an artificial PHC due to the spinning water-filled prism; panel (d) the BK7 glass PHC for comparison.

[a]Electronic mail: markus.selmke@gmx.de

[1]W. Tape, *Atmospheric Halos* (American Geophysical Union, Washington, 1994).
[2]W. Tape and J. Moilanen, *Atmospheric Halos and the Search for Angle x* (American Geophysical Union, Washington, 2006).
[3]L. Cowley, "Atmospheric optics web site," <http://www.atoptics.co.uk>.
[4]L. Cowley and M. Schroeder, "HaloSim simulation program," <http://www.atoptics.co.uk/halo/halfeat.htm>.
[5]J. D. Walker, "Multiple rainbows from single drops of water and other liquids," Am. J. Phys. **44**(5), 421–433 (1976).
[6]G. Casini and A. Covello, "The 'rainbow' in the drop," Am. J. Phys. **80**(11), 1027–1034 (2012).
[7]J. I. Katz, "Subsuns and low Reynolds number flow," J. Atmos. Sci. **55**, 3358–3362 (1998).
[8]D. K. Lynch and W. Livingston, *Color and Light in Nature* (Cambridge U.P., Cambridge, 2001).
[9]A. Bravais, "Mémoire sur les halos et les phénomènes optiques qui les accompagnent," J. de l' École Royale Polytechnique **31**(18), 1–270 (1847).
[10]M. Élie de Beaumont, *Memoir of Auguste Bravais* (Smithsonian Institution, Washington, 1869).
[11]A. Wegner, "Die nebensonnen unter dem horizont," Meteorol. Z. **34–52**(8/9), 295–298 (1917).
[12]M. V. Berry and S. Klein, "Diffraction near fake caustics," Eur. J. Phys. **18**, 303–306 (1997).
[13]M. Vollmer and R. Tammer, "Laboratory experiments in atmospheric optics," Opt. Express **37**(9), 1557–1568 (1998).
[14]M. Vollmer and R. Greenler, "Halo and mirage demonstrations in atmospheric optics," Appl. Opt. **42**(3), 394–398 (2003).
[15]M. Großmann, K.-P. Moellmann, and M. Vollmer, "Artificially generated halos: Rotating sample crystals around various axes," Appl. Opt. **54**(4), B97–B106 (2015).
[16]J. A. Lock and J. H. Andrews, "Optical caustics in natural phenomena," Am. J. Phys. **60**(5), 397–407 (1992).
[17]J. A. Adam, "The mathematical physics of rainbows and glories," Phys. Rep. **356**, 229–365 (2002).
[18]M. V. Berry, "Supernumerary ice-crystal halos?," Appl. Opt. **33**(21), 4563–4568 (1994).
[19]D. Brewster, *A Treatise on Optics* (Longman, Rees, Orme, Brown & Green, London, 1831).
[20]A. Cornu, "Sur la reproduction artificielle des halos et des cercles parhéliques," Comtes Rendus Ac. Paris **108**, 429–433 (1889).
[21]H. Masui, S. Nakamura, and S. P. DenBaars, "Analytical light-ray tracing in two-dimensional objects for light-extraction problems in light-emitting diodes," Appl. Opt. **47**(1), 88–92 (2008).
[22]M. N. Polyanskiy, "Refractive index database," <www.refractiveindex.info>.
[23]G. P. Können, "Polarization and intensity distributions of refraction halos," J. Opt. Soc. Am. **73**(12), 1629–1640 (1983).
[24]Processing web site, <www.processing.org>.
[25]See supplemental material at http://dx.doi.org/10.1119/1.4923458 for photographs, animations, and simulation software.
[26]M. Sillanpää, J. Moilanen, M. Riikonen, and M. Pekkola, "Blue spot on the parhelic circle," Appl. Opt. **40(30)**, 5275–5279 (2001).
[27]G. H. Liljequist, *Halo-Phenomena and Ice-Crystals*, Norwegian-British-Swedish Antarctic Expedition 1949–52 Vol. 2 (Norsk Polarinstitutt, Oslo, 1956).
[28]E. B. Saff and A. B. J. Kuijlaars, "Distributing many points on a sphere," Math. Intell. **19**(1), 5–11 (1997).
[29]The paraxial focal length of a thin shell is $1/f \approx \delta r(1-n)/r^2$, with r, δr, and n being the radius, the thickness, and the refractive index of the sphere, respectively. For the sphere used in the experiment, this amounts to a weakly divergent lens with $f \sim -10$ m.
[30]Adafruit (online electronics retailer), <www.adafruit.com>.
[31]D. S. Lemons, *An Introduction to Stochastic Processes in Physics* (The Johns Hopkins U.P., Baltimore, 2002).
[32]Any quantitative assessment requires the linear intensity data, which can be extracted from raw files using software such as MakeTiff, C F Systems, <http://www.colorneg.com/MakeTiff/>.
[33]Reinhard Selmke, Private communication (2014).
[34]U. Griesmann, Q. Wang, J. Soons, and R. Carakos, "A simple ball averager for reference sphere calibrations," Proc. SPIE **5869**, 58690S (2005).
[35]W. J. Humphreys, *Physics of the Air*, 3rd ed. (Dover Publications, New York, 1965).
[36]S. Borchardt and M. Selmke, "Intensity distribution of the parhelic circle and embedded parhelia at zero solar elevation: theory and experiments," Appl. Opt. **54**(22), 6608–6615 (2015).
[37]Z. Ulanowski, "Ice analog halos," Appl. Optics **44**(27), 5754–5758 (2005).
[38]G. P. Können, "A note on the radiance distributions of halos due to scattering by randomly orientated crystals," Appl. Opt. **54**(4), B177–B184 (2015).